

RESEARCH ARTICLE

10.1029/2017JD027785

Key Points:

- This study quantifies the sensitivity and uncertainty in global, terrestrial estimates of sensible heat flux due to the input data sets
- The largest sensitivity and uncertainty is found in the Amazon, Indonesia, northern Australia, and the plains of North America
- The global average uncertainty in sensible heat flux is 24.8 W/m^2 , primarily due to the influence of the temperature gradient

Correspondence to:

 A. L. Siemann,
 siemann@princeton.edu

Citation:

 Siemann, A. L., Chaney, N., & Wood, E. F. (2018). Sensitivity and uncertainty of a long-term, high-resolution, global, terrestrial sensible heat flux data set. *Journal of Geophysical Research: Atmospheres*, 123, 4988–5000. <https://doi.org/10.1029/2017JD027785>

Received 25 SEP 2017

Accepted 6 FEB 2018

Accepted article online 6 MAY 2018

Published online 18 MAY 2018

Sensitivity and Uncertainty of a Long-Term, High-Resolution, Global, Terrestrial Sensible Heat Flux Data Set

 Amanda L. Siemann¹ , Nathaniel Chaney¹ , and Eric F. Wood¹ 
¹Department of Civil and Environmental Engineering, Princeton University, Princeton, NJ, USA

Abstract Sensible heat flux directly influences local and regional climate and can be estimated using remotely sensed satellite observations. Although significant efforts have been made to estimate sensitivity and uncertainty in energy flux estimates at the local and regional scales using both models and algorithms compatible with remotely sensed satellite data, few studies quantify the sensitivity or uncertainty at the global scale, enabling a global comparison among uncertainty drivers. This study uses the 10 percentile change from the mean value in the empirical cumulative distribution function for the distribution of each input data set to calculate the sensitivity of the unconstrained, terrestrial sensible heat flux to change in the input data sets and uses this sensitivity in a first-order analysis of the uncertainty in the sensible heat flux. The largest sensitivities to the Zilitinkevich empirical constant (C_{z11}) are in the Amazon, northern Australia, and the plains of North America, while the sensitivity of the sensible heat flux to the temperature gradient is largest in dry regions of shorter vegetation. The C_{z11} contributes most to the uncertainty of over $50\text{--}100 \text{ W/m}^2$ in the Amazon and Indonesia, while the temperature gradient contributes most to the uncertainty elsewhere, producing an overall global average uncertainty of 24.8 W/m^2 . Future work should reduce the uncertainties in the temperature gradient and the C_{z11} to reduce the uncertainty in sensible heat flux estimates.

1. Introduction

The turbulent fluxes of latent and sensible heat at the Earth's surface drive local and regional climate. Through these fluxes, the available energy at the land surface is apportioned into water and heat conduction (Pipunic et al., 2008). Among the options for measuring these fluxes, satellite remote sensing offers increased coverage for global estimates (Jimenez et al., 2011) compared with local eddy covariance measurements (e.g., FLUXNET web page, 2016) and field campaigns (e.g., the Boreal Ecosystem-Atmosphere Study, Sellers et al., 1997). Siemann et al. (2018) developed and validated global, terrestrial, 0.5° resolution sensible heat flux products using remotely sensed satellite observations, and in this study, we analyze the sensitivity and uncertainty in the global unconstrained estimates.

Although various studies explore and quantify uncertainty of estimated energy fluxes relative to independent observations (e.g., Chehbouni et al., 2001; Oleson & Bonan, 2008; Wang et al., 2016) or relative to a regional reference data set of higher accuracy when using different data sets for a given input (Madhusoodhanan et al., 2017), several other studies quantify sensitivity and uncertainty of energy and water fluxes inherent in their estimation. Xu et al. (2017) and Jung et al. (2011) quantify uncertainty in regional or global energy flux estimates, respectively, upscaled from tower-observed fluxes using, in Xu et al. (2017), uncertainty within the algorithms used to upscale these estimates, including instrument uncertainty, state variable uncertainty, turbulent sampling random and systematic uncertainty, and training uncertainty, and using the standard deviation of model trees from a machine learning algorithm used as estimators in Jung et al. (2011). While these uncertainties incorporate uncertainties from various features within the models, neither of these studies explicitly assess the sensitivities within the fluxes. Zhang et al. (2017) and Rosolem et al. (2012) implement the Sobol sensitivity analysis method to the Priestly-Taylor evapotranspiration model from National Aeronautics and Space Administration's Jet Propulsion Laboratory and the Simple Biosphere 3 model, respectively, to calculate the sensitivity indexes and compare the sensitivity of the output fluxes to the parameters within the models. Additionally, studies such as Bormann (2008) and Long et al. (2011) vary the spatial resolution of inputs to determine the impact of resolution on the estimated fluxes compared to a reference model simulation.

Other sensitivity analysis approaches use Monte Carlo-based methods to calibrate parameters within models used to calculate energy fluxes and examine the sensitivity of the fluxes. Schulz and Beven (2003) uses a

Bayesian Monte Carlo framework within the generalized likelihood uncertainty estimation method to calibrate the parameters for and compute uncertainty bounds on predictions from different soil vegetation atmosphere transfer models for estimating latent heat flux. Hou et al. (2012) applies a minimum relative entropy approach, which is a quasi-Monte Carlo method, to generate the values for the parameters using prior probability distribution functions to quantify uncertainty and sensitivity in the Community Land Model at 13 flux tower sites in the United States. Metzger et al. (2016) also uses a Monte Carlo-based sensitivity analysis to assess the impact of 54 parameters on outputs of water and heat fluxes in the Coupled heat and mass transfer model for the soil-plant-atmosphere system (CoupModel) version 5 using 50,000 runs.

In addition to adjusting parameters to incorporate the sensitivity and uncertainty resulting from changes in those parameters, the uncertainty from input data, and how that uncertainty propagates into the resulting energy flux estimates from the different data sets required to calculate the estimates needs to be evaluated (Bormann, 2008). Uncertainty increases when input data needs to be taken from several sources (Bounoua et al., 2006), as is the case for energy flux algorithms requiring both global meteorological data as well as land cover properties. Boisier et al. (2012) uses multivariate regression analysis of seasonal anomalies in energy fluxes with those of input land cover variables to determine the sensitivity of the global climate models to these changes. Instead of looking at historical changes in the inputs, several studies perturb input variables by set increments to analyze the sensitivity and uncertainty in energy fluxes produced by these perturbations. Dirmeyer et al. (2000) uses fractions of the soil wetness index of 0.05, 0.1, 0.25, and 0.5 to determine the sensitivity of the evaporative fraction to this index. Alton et al. (2006) varies meteorological inputs such as specific air humidity, surface pressure, wind speed, and air temperature within the limits of uncertainty in each, defined to be $\pm 10\%$, $\pm 5\%$, $\pm 10\%$, and $\pm 0.33\%$, respectively, based on tower observations, to assess the sensitivity and uncertainty in energy fluxes from the Joint United Kingdom Land Environment Simulator model.

Many of the above studies assess the sensitivity and uncertainty in land models or climate models, but other studies examine sensitivity and uncertainty in algorithms based on remotely sensed satellite data. Cammalleri et al. (2012) synthetically alters the radiative surface temperature by 1 °K and 3 °K, determined from the 1 °K uncertainty in the remotely sensed surface temperature, to determine the sensitivity of the two-source energy balance (TSEB) model to potential errors in temperature. Sanchez et al. (2008) calculates the sensitivity in the simplified two-source energy balance model by increasing and decreasing the input data for the whole time series by the uncertainty in that input, which Sanchez et al. (2008) defines as 50% uncertainty for roughness length for momentum, 10% uncertainty for wind speed, and 1–2°C for land surface temperature (LST), for example, while holding the rest of the input data at the reference values. The difference in the fluxes output from simplified two-source energy balance are then normalized by the reference value for the input adjusted to obtain the relative sensitivity, which is averaged over the time series. Using a similar methodology to calculate sensitivity, Timmermans et al. (2007) applied changes of 1.25% and 0.75% to the input data to calculate the sensitivities but used only 1% changes for the surface temperature to remain within a reasonable range of temperatures, while Long et al. (2011) perturbed the input data and parameters derived from Moderate Resolution Imaging Spectroradiometer (MODIS) images for use in TSEB as well as the Surface Energy Balance Algorithm for Land by 5% increments within $\pm 50\%$ for each input but used a 2 °K increment for LST. Marx et al. (2008) not only calculates the sensitivity in sensible heat flux derived from satellites but also calculates the uncertainty due to the input data using a method based on Gaussian Error Propagation in which the variance of sensible heat flux is calculated as the sum over all inputs of the squared sensitivity of sensible heat flux to a given change in one input times the square of the standard deviation of that input. Also, Tang et al. (2013) have quantified the uncertainty of the Surface Energy Balance Algorithm for Land model caused by variation in the sizes of the area of interest and satellite pixel on estimating the regional sensible heat flux and latent heat flux by proposing generalized analytical equations and through model applications.

Although the strategies to compute sensitivity and uncertainty in energy fluxes, such as sensible heat flux, differ among studies, many of the studies mentioned above have narrow domains of the local tower or in situ station scale (e.g., Alton et al., 2006; Cammalleri et al., 2012; Chehbouni et al., 2001; Marx et al., 2008; Sanchez et al., 2008), catchment scale (e.g., Metzger et al., 2016; Long et al., 2011; Wang et al., 2016), or the regional scale (e.g., (Boisier et al., 2012; Bounoua et al., 2006; Hou et al., 2012; Timmermans et al., 2007), with only

Jung et al. (2011) at the global scale. Additionally, several of these studies evaluate a lengthy list of parameters, but the most commonly examined parameters and input data sets for sensible heat flux estimates examined are temperatures (e.g., Alton et al., 2006; Chehbouni et al., 2001; Cammalleri et al., 2012; Long et al., 2011; Marx et al., 2008; Sanchez et al., 2008; Timmermans et al., 2007; Xu et al., 2017; Zhan et al., 1996), including the temperature gradient between the LST and the air temperature (e.g., Gibson et al., 2011), wind speed (e.g., Alton et al., 2006; Long et al., 2011; Marx et al., 2008; Sanchez et al., 2008; Timmermans et al., 2007; Zhan et al., 1996), and the aerodynamic properties of the vegetation such as the roughness length for momentum (e.g., Long et al., 2011; Marx et al., 2008; Sanchez et al., 2008; Timmermans et al., 2007; Xu et al., 2017; Zhan et al., 1996), leaf area index (e.g., Alton et al., 2006; Sanchez et al., 2008; Timmermans et al., 2007; Zhan et al., 1996), a vegetation index such as normalized difference vegetation index (e.g., Timmermans et al., 2007; Zhan et al., 1996) or the enhanced vegetation index (e.g., Xu et al., 2017), or displacement height and fractional vegetation cover (e.g., Tang et al., 2010; Tang & Li, 2017).

In this study, we quantify the global scale sensitivity of the sensible heat flux due to the dominant input data sets of the temperature gradient between the surface and the atmosphere, and the input data for the aerodynamic resistance including the wind speed, the roughness length for momentum, and the C_{zil} empirical constant defined below in equation (10). We then use this sensitivity to calculate the global uncertainty in the sensible heat flux due to these input data sets with a method similar to the methodology of Marx et al. (2008). For the sensitivity calculation, instead of applying a percentage change from the mean value for each input, we calculate the 10th percentile change in the empirical cumulative distribution function (ECDF) for the distribution of each data set, grouped either by vegetation height or by latitude, and use this value for the change from the mean for the full time series for each input, and we average the resulting change in the sensible heat flux over the full time series for each pixel, globally. Although the methodology, in itself, is not significantly novel, in this study, we apply it globally, enabling us to compare the drivers of the sensitivity and uncertainty in the sensible heat flux at this global scale. We present the sensitivity of the sensible heat flux to each input in section 3.1, and we present the uncertainty due to each input as well as the overall uncertainty in the sensible heat flux in section 3.2. The results are discussed in sections 4.1–4.2.

2. Data and Methods

2.1. Sensitivity Analysis

In this study, we compute the sensitivity of the sensible heat flux to each of the dominant input variables by a first-order Taylor expansion of the function for sensible heat flux, $g(x)$, at the mean, \bar{x} , as follows

$$g(x) = g(\bar{x}) + g'(\bar{x}) \times (x - \bar{x}) \quad (1)$$

We define the sensitivity of the sensible heat flux to changes in input variables as $g'(\bar{x})$, which is the differential of $g(x)$ with respect to x evaluated at \bar{x} , and can be estimated using a centered difference approximation (Chapra & Canale, 2010)

$$g'(\bar{x}) = \frac{g(\bar{x} + \Delta x) - g(\bar{x} - \Delta x)}{2\Delta x} \quad (2)$$

in which Δx is the change in the variable x from \bar{x} . Because this symmetric difference quotient is derived from a linear approximation of the function, it is not a sufficient approximation of the slope due to the nonlinearities in $g(x)$. Therefore, we use a more accurate estimate of the slope as follows

$$g'(\bar{x}) = \frac{g(\bar{x} + \Delta x) - g(\bar{x} - \Delta x)}{2\Delta x} + \bar{x} \times g''(\bar{x}) \quad (3)$$

accounting for the second derivative using the centered difference approximation as follows (Chapra & Canale, 2010)

$$g''(\bar{x}) = \frac{g(\bar{x} + \Delta x) - 2g(\bar{x}) + g(\bar{x} - \Delta x)}{(\Delta x)^2} \quad (4)$$

If we had a continuous function for $g(x)$, the derivatives could be computed at $g(\bar{x})$. Rather they are computed numerically using the above equations. Although the magnitudes of the variables are different, we use a Δx

Table 1
Changes Around the Mean for Sensitivity Analysis Inputs

| Vegetation Category | C_{zil} | Roughness length (s/m) |
|---------------------|---------------------------|------------------------|
| Tall | 0.035 | 0.020 |
| Short | 0.041 | 0.004 |
| Latitude Region | Temperature gradient (°K) | Wind speed (m/s) |
| Tropics | 0.538 | 0.376 |
| Extratropics | 0.628 | 0.457 |
| High latitudes | 0.669 | 0.508 |

Note. These changes around the mean are the Δx values in section 2.1 determined from the average difference between the 40th and 50th percentiles and 50th and 60th percentiles in the empirical cumulative distribution function of the distributions.

relative to the ECDF for each variable, respectively, by taking the average of the difference between the 40th and 50th percentile and the difference between the 50th and 60th percentile in the ECDF. These intervals are large enough to capture the nonlinear changes in $g(x)$ away from the mean, but not so large as to distort the approximation of $g(x)$ in ((2)) and ((4)). For the temperature gradient and wind speed, we compute the ECDF for three latitudinal zones, the tropics (20°S–20°N), extratropics (21°S–40°S and 21 N–40 N), and high latitudes (41°S–90°S and 41 N–90 N) by averaging the ECDF obtained from 10 sets of 10,000 randomly selected land grid values, without replacement. For the C_{zil} and roughness length, we compute the ECDF for short (including closed and open shrubland, savannahs, grasslands, and cropland land cover types) and tall (including needleleaf forests, broadleaf forests, mixed forests, and

woody savannah land cover types) vegetation separately by using all grids with over 99.9% coverage for the respective land cover types in each category. The Δx values computed from the respective ECDFs are shown in Table 1.

We compute the sensitivity by computing the sensible heat flux full time series (i.e., hourly, from 1979 to 2009) for each grid, globally, using the mean values for C_{zil} and roughness length and the full time series for all time-varying inputs, and changing one dominant input at a time for the full time series. We, then, calculate the average change in sensible heat flux ascribed to the change in each variable from the full time series to obtain the sensitivity for each grid.

2.2. Uncertainty Analysis

The sensitivity of sensible heat flux to each of its dominant inputs enables us to calculate the overall uncertainty in the sensible heat flux estimates using the first-order analysis of uncertainties. If we use the first-order approximation of the function $H = g(x)$, where $g(\cdot)$ is the function describing H , x is a vector of k uncertain input variables (in our case $k = 4$), then we can approximate the variance of H as (Mays & Tung, 1992, equation 5.3.3.)

$$\text{Var}[H] = \text{Var}\left[g\left(\bar{x}\right)\right] + \sum_i^k \sum_j^k \left[\frac{\Delta g}{\Delta x_i}\right] \left[\frac{\Delta g}{\Delta x_j}\right] \text{Cov}(x_i, x_j) \quad (5)$$

where $\left[\frac{\Delta g}{\Delta x_i}\right]$ is the sensitivity coefficient representing the rate of change in the function $g(x)$ at $x = \bar{x}$ for input parameter x_i . Because the approximation of $g(x)$ is around the mean values of \bar{x} , the $\text{Var}[g(\bar{x})]$ term is 0.

We acknowledge that the input variables could be correlated, so we calculated the correlation coefficients among the data sets. The correlation coefficients rarely rise above 0.5, so we simplifying equation (5) by assuming that these variables are uncorrelated leading to (Mays & Tung, 1992)

$$\text{Var}[H] = \sum_{i=1}^k \left[\frac{\Delta g}{\Delta x_i}\right]_{\bar{x}}^2 * \text{Var}[x_i] \quad (6)$$

For the temperature gradient, we calculate the sample variance of the average difference between the hourly temperature gradient using the Wang and Zeng (2013) air temperature formed from the European Centre for Medium-Range Weather Forecasts reanalysis-Interim project data and the five remaining hourly temperature gradients for the full time period to obtain the variance in the temperature gradient. We calculate the sample variance of the average difference between 3-hourly Climate Forecast System Reanalysis (CFSR) wind speed and two other 3-hourly wind speed data sets, the Modern-Era Retrospective analysis for Research and Applications and the Princeton Global Forcing data set version 1 (Sheffield et al., 2006). We calculate the variance in C_{zil} from the standard deviation computed from the 8,500 decision tree predictions within the fitted Extra-Trees model for each grid, ranging from 0.04 to 0.18 (Chaney et al., 2016). We also assume a variance of 10% of the squared averaged roughness value for each grid, using the weighted average of roughness based on fractional area for each vegetation type. This choice of 10% of the squared roughness length as the

variance is similar to the choice by Marx et al. (2008) to use 10% of the roughness length as the standard deviation of this input in their uncertainty calculation.

2.3. Sensible Heat Flux Methodology

2.3.1. First-Order Approximation

The sensible heat flux (H) is described in detail in Siemann et al. (2018). We parameterized the sensible heat flux with the first-order approximation according to Monteith (1973)

$$H = \frac{\rho C_p (T_s - T_a)}{r_a} \quad (7)$$

where T_s is the physical LST calculated with the High-Resolution Infrared Radiation Sounder (HIRS) LST (°K) computed in Coccia et al. (2015) and evaluated in Siemann et al. (2016) and MODIS emissivity (the HIRS-consistent LST assumes an emissivity of 1.0), T_a is the potential air temperature calculated with a 2-m air temperature (°K), ρ (kg/m^3) is the air density calculated using the National Oceanic and Atmospheric Administration's CFSR (Saha et al., 2010) air pressure at the 2-m air temperature, C_p is the specific heat capacity of air at constant pressure ($1,004.6 \text{ J}\cdot\text{kg}^{-1}\cdot\text{K}^{-1}$), and r_a is the aerodynamic resistance (s/m). $T_s - T_a$ is the surface temperature gradient, and we modify it as an input variable for the sensitivity and uncertainty analysis instead of prescribing each temperature separately (as further discussed in Siemann et al., 2018). The sensible heat flux is also calculated at 0.5° , hourly resolution in this analysis. Siemann et al. (2018) validated the products calculated with this methodology against both FLUXNET estimates as well as at the basin scale using inferred sensible heat flux from precipitation, runoff, net radiation, and ground heat. Sections 2.3.2–2.3.3 describe the data sets used for the temperatures as well as the methodology for r_a .

2.3.2. Surface Temperature Gradient

The physical LST, T_s , was calculated using the hourly, 0.5° resolution LST product over the period 1979–2009 developed by Coccia et al. (2015) to be consistent with HIRS satellite retrievals. Coccia et al. (2015) binned the retrievals into hourly time steps, aggregated them to 0.5° resolution grids, and used the Model Conditional Processor (Coccia & Todini, 2011; Todini, 2008) Bayesian methodology to merge CFSR estimates with the satellite retrievals, averaging the resulting merged data sets using the linear opinion pool approach (Clemen & Winkler, 1999; Stone, 1961). Siemann et al. (2016) validated this LST product against a LST derived using Baseline Surface Radiation Network measured upward longwave radiation with the Stefan-Boltzmann Law. To calculate the physical LST, Siemann et al. (2018) adjusted this LST by the monthly MODIS emissivity for the 14 MODIS University of Maryland vegetation types (Ren et al., 2013).

To form the temperature gradient, Siemann et al. (2018) used six-hourly, global, 0.5° resolution 2-m air temperature data sets for 1979–2009 for the six sensible heat products corresponding with each air temperature. In this study and based on the results presented in Siemann et al. (2018), we use the CFSR air temperature product as the mean air temperature to form the temperature gradients with the HIRS-consistent LST, and we adjust the temperature gradient as one of the input variables for the sensible heat flux.

2.3.3. Aerodynamic Resistance

We follow the methodology in Siemann et al. (2018) based on Monteith's (1973) parameterization for the sensible heat flux. We group the aerodynamic resistance as follows

$$r_a = \frac{1}{C_h u_z} \quad (8)$$

where the u_z is the wind speed from CFSR (ms^{-1}) and the C_h is the coefficient of heat transfer. Ek et al. (2003) describes the parametrization used in the offline Noah Land Surface Model version 3.4.1 which uses the Janjic (1994) formulation to calculate for the C_h as follows

$$C_h = \frac{u_* k}{\left[\ln\left(\frac{z+z_{0m}}{z_{0h}}\right) + \Psi_h\left(\frac{z+z_{0m}}{L}\right) - \Psi_h\left(\frac{z_{0h}}{L}\right) \right]} \quad (9)$$

where k is the von Karman constant, z is the reference height (m), u_* is the friction velocity (m/s), L is the Obukhov length (Monin & Obukhov, 1954), and z_{0h} and z_{0m} are the roughness lengths for heat and momentum (m). We use the z_{0m} from the University of Maryland land cover type data set (Defries et al., 2000) for 14 land cover types upscaled from $\sim 1 \text{ km}$ to 0.5° resolution (see Hansen et al., 2000, for detailed description of each type), and in this study, we compute the area weighted average z_{0m} to be used as the mean value. The

following relationship is also applied between the two roughness lengths to correct for the difference between the near surface air temperature and the radiative skin temperature (used as the LST)

$$\frac{z_{0m}}{z_{0h}} = \exp\left(kC_{z0l}\sqrt{Re^*}\right) \quad (10)$$

where Re^* is the roughness Reynolds number and C_{z0l} is first defined in Zilitinkevich (1995). In this study, we use the data set developed by Chaney et al. (2016) for the mean C_{z0l} value. The wind speed, z_{0m} , and C_{z0l} are adjusted for the sensitivity analysis from the mean values according to section 2.1.

3. Results

3.1. Sensitivity of Sensible Heat to Inputs

Figure 1 displays the overall sensitivity of sensible heat flux to changes in C_{z0l} , temperature gradient, surface roughness, and wind speed, respectively, in panels a, b, c, and d. The largest sensitivity to change in C_{z0l} (Figure 1a) occurs within 300–350 W/m² change per unit of C_{z0l} in the Amazon, northern Australia, the plains of North America, and some regions of Africa and Eurasia. In Figure 1b, the largest sensitivity to the surface temperature gradient is within 8–20 W/m² change per degree kelvin in temperature gradient in central Eurasia, the northern plains of North America, the Sahara, the Middle East, South Africa, and Australia. Some similar areas, such as the Sahara, the Middle East, central Eurasia, Australia, and the plains of North America share a large sensitivity to the roughness length (Figure 1c) in the range of 200–500+ W/m² change per meter change in roughness length. The smallest sensitivity to the roughness length in the range of 1–10 W/m² is concentrated in the tropics as well as areas of northern Canada and some high latitudes of Eurasia. In Figure 1d, the largest sensitivity to the wind speed in the range of 8–30 W/m² change per 1 m/s of wind speed occurs in the Sahara, the Middle East, and Australia. Similar regions of the tropics and northern high latitudes shown in Figure 1c have the smallest sensitivity to change in wind speed of under 2 W/m² in the high latitudes and part of the Congo but also under 6 W/m² in the Amazon. While the largest relative sensitivities are distributed differently among the inputs, some of the smallest relative sensitivities can consistently be found in the northern high latitudes.

3.2. Uncertainty in Sensible Heat Due to Uncertainty in Inputs

Using the sensitivity to calculate uncertainty in sensible heat due to each input, we calculate the overall uncertainty in sensible heat due to the combination of these four dominant inputs, displayed in Figure 2. The largest uncertainty of 35–200 W/m² in sensible heat flux occurs in the Amazon, while the smallest uncertainty of 5–10 W/m² occurs in the northern middle to high latitudes. Although the Amazon, parts of Indonesia, and the Congo have similar land cover types, the uncertainty in the Amazon and parts of Indonesia is far larger than the uncertainty in the Congo, which is only 5–15 W/m². In Figure 2, the remainder of the globe displays at least 5 W/m² uncertainty, and most commonly between 25 and 35 W/m². The overall global average uncertainty is 27.4 W/m².

Figure 3 shows the fraction of the total uncertainty attributed to each input. Uncertainty due to the temperature gradient (Figure 3b) dominates in most regions, particularly in the northern high latitudes, but the uncertainty due to the C_{z0l} (Figure 3a) dominates in the Amazon and areas of Indonesia, the eastern continental United States (CONUS), and eastern Asia, which are tropical and midlatitude forested regions. The wind speed (Figure 3d) contributes the least to the uncertainty with all fractions of the total under 0.3 and under 0.1 in most regions.

Figure 4 provides additional context by displaying both the relative uncertainty, defined as the uncertainty due to each input normalized by the mean (the unconstrained product using the CFSR air temperature from Siemann et al., 2018) in panels a–d, as well as the coefficient of variation, depicting the standard deviation normalized by the mean in panel e. The relative uncertainty due to the C_{z0l} in Figure 4a is largest (above 0.5) in the Amazon, eastern CONUS, central Africa, much of Europe, and southeast Asia. The relative uncertainty due to the temperature gradient in Figure 4b is largest (above 5–10) in the northern high latitudes and is smallest in the Sahara, the Middle East, the Horn of Africa, and Australia. The relative uncertainty due to the roughness length is under 0.2 in all regions except the southern half of South America and Africa, while the relative uncertainty due to the wind speed in Figure 4d is under 0.1 across most of the globe. In Figure 4e, the Amazon and northern high latitudes have the largest coefficients of variation of well over 1.0

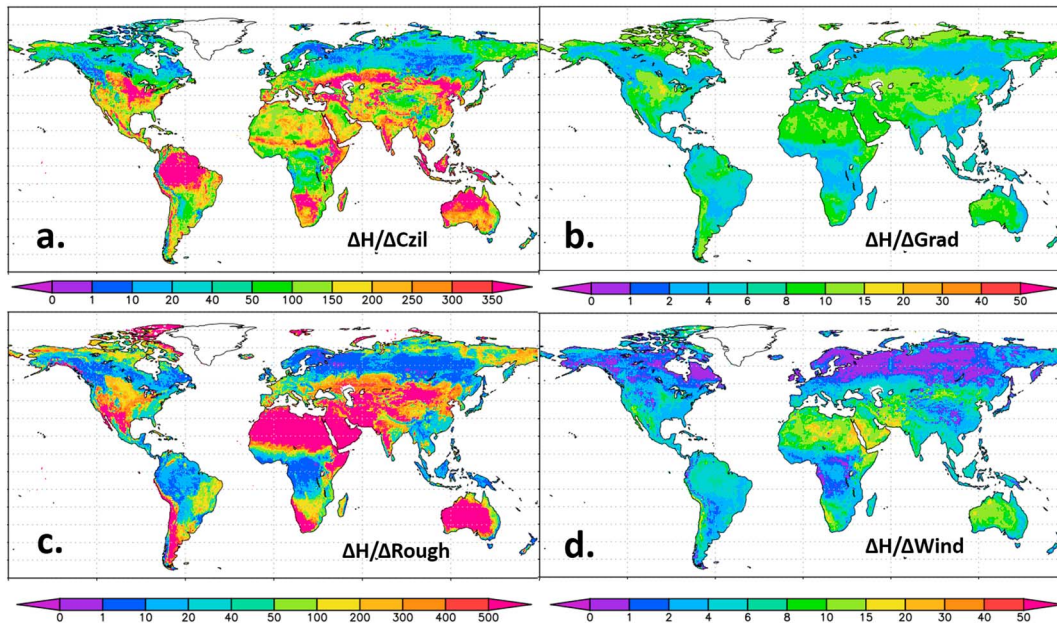


Figure 1. Total sensitivity of sensible heat flux to changes in C_{zil} , temperature gradient (grad), surface roughness (rough), and wind speed, respectively in panels a–d. Units are change in watt per square metre per change in C_{zil} (unitless), per change in temperature gradient in degrees kelvin, per change in roughness length in meters, and per change in wind speed in meters per second.

in some regions. The lowest coefficients of variation of 0.1–0.3 occur in the Sahara, the Horn of Africa, the Middle East, most of Australia, and India, among other smaller regions.

4. Discussion

4.1. Sensitivity Analysis

In Figure 1a displaying the sensitivity of sensible heat flux to a unit change in C_{zil} , we find the largest sensitivities of over 350 W/m^2 in both regions of tall vegetation such as the forests of the Amazon and drier regions of shorter vegetation such as the upper Midwest of CONUS, Canadian plains, northern Australia, and some regions of Africa and Eurasia. We find sensible heat flux sensitivity to C_{zil} in regions of South America, Africa,

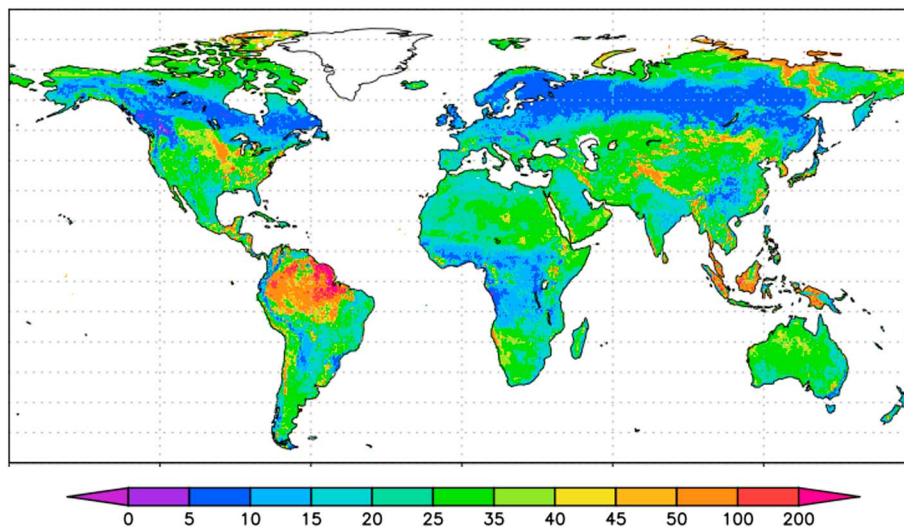


Figure 2. Total uncertainty in sensible heat due to the dominant inputs of C_{zil} , roughness length, temperature gradient, and wind speed. This uncertainty is the square root of the sum of the variances in each input which are calculated using the sensitivity of sensible heat to each component and the uncertainty in each component.

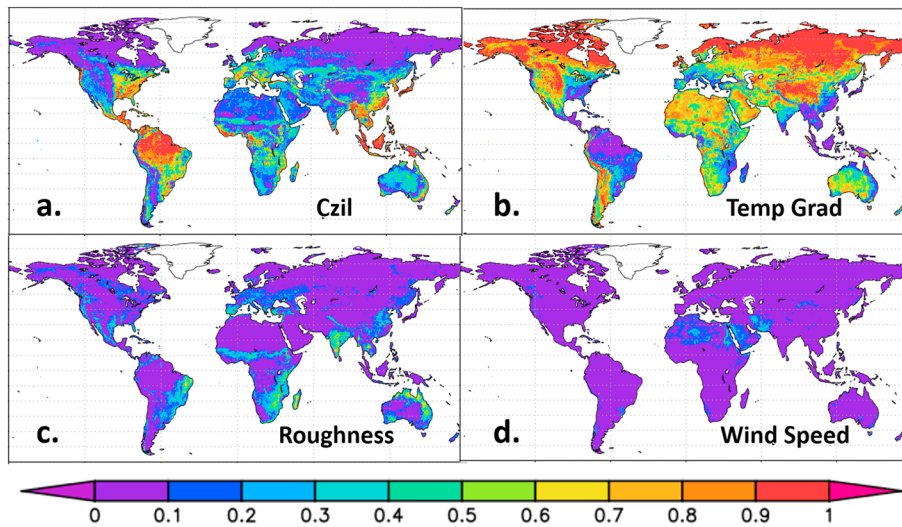


Figure 3. Fraction of the total uncertainty in the sensible heat flux due to each dominant input of C_{zil} , temperature gradient, surface roughness length and wind speed in panels a–d, respectively.

and Asia that do not have many FLUXNET eddy flux towers because the C_{zil} is first fitted at available flux towers and extended globally based on land cover and climate covariates (see Chaney et al., 2016, for further details). C_{zil} in regions without towers is more uncertain. As for the upper Midwest of CONUS and Canadian Plains, the relative abundance of eddy flux towers to which the C_{zil} was fit can result in quite different (and more variable) C_{zil} estimates relative to areas with fewer towers, producing larger sensible heat flux sensitivities.

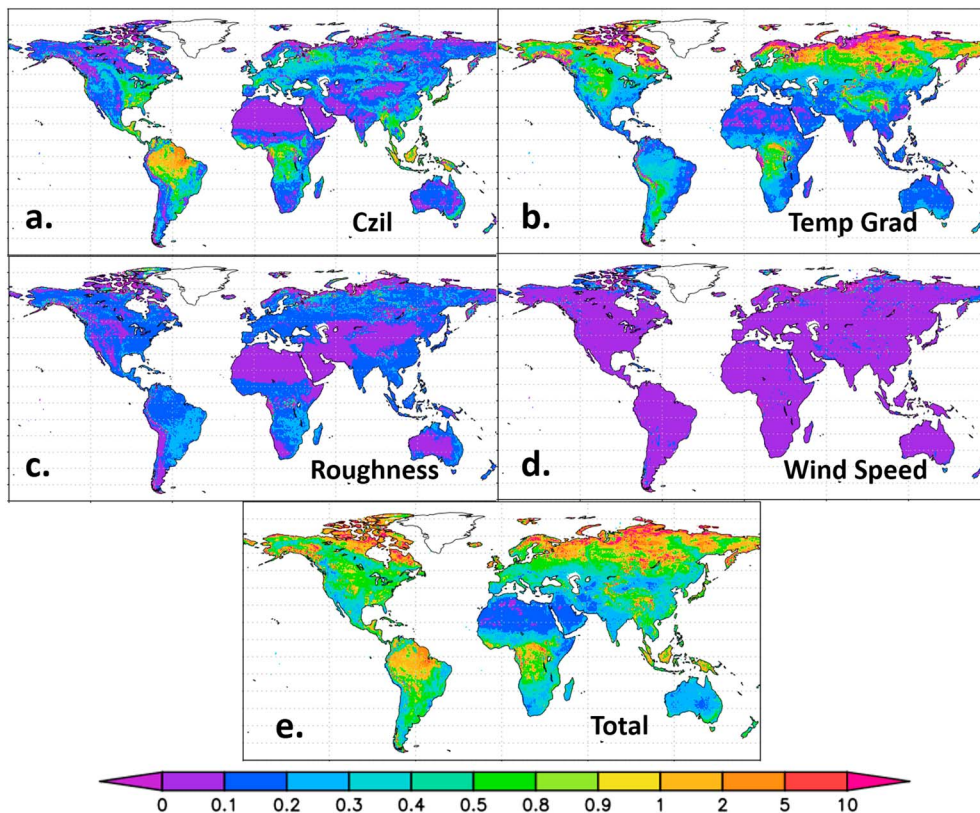


Figure 4. The relative uncertainty due to each input (uncertainty due to each input normalized by mean sensible heat flux of the product using the Climate Forecast System Reanalysis air temperature) including C_{zil} , temperature gradient, roughness length, and wind speed in panels a–d, respectively, and the coefficient of variation, calculated as the standard deviation normalized by the mean of the sensible heat flux in panel e.

In Figure 1b, the largest sensitivities of 10–20 W/m² per 1 °K change in the temperature gradient are in the upper Midwest of CONUS, Canadian plains, central Eurasia, and portions of the Sahara, South Africa, and Australia. These regions all contain shorter vegetation such as grassland or bare soil land cover, which are typically dry. As mentioned in Siemann et al. (2018), these regions exhibit high sensible heat fluxes, as more available energy is partitioned into sensible heat flux instead of latent heat flux due to the lack of taller vegetation and sometimes lack of moisture. The sensitivity of sensible heat flux may be higher to the temperature gradient in these regions also because the aerodynamic resistance is lower relative to other regions, and when the resistance is small relative to the size of the gradient, any change in gradient will produce a drastically different estimate of sensible heat flux. Although no other studies have completed a global sensitivity analysis of the response of our first-order parameterization for sensible heat flux to changes in the temperature gradient, Norman et al. (1995) estimated local change in sensible heat flux calculated with TSEB can approach 90 W/m² with 1 °K change in the gradient at locations with taller vegetation, so our estimates are well within this range when using our sensible heat flux parameterization.

The largest sensitivities in Figure 1c of the sensible heat flux to roughness length are in short vegetation regions such as the southwest CONUS, Australia, the Middle East, and the Sahara, and the smallest sensitivities are in forested regions such as the Amazon, the Congo, and portions of Canada. The larger sensitivity to changes in roughness length occurs when the roughness lengths are small and is likely because a unit change in the roughness length (i.e., by 1 m) could more than double or triple the given roughness length in those regions, which, for example, have a roughness length of 0.0112 m for bare soil, causing a drastically different aerodynamic resistance that significantly changes the sensible heat flux. At larger roughness lengths, as in forested areas with a roughness length of 2.653 m such as the Amazon evergreen broadleaf forests, the roughness is already large that the change in resistance it produces is not big enough to make an impact compared to the magnitude of the larger aerodynamic resistance it produces.

Larger sensitivity to wind speeds in northern Africa, the Middle East, and Australia as seen in Figure 1d occurs in drier regions. In these dry regions with low lying vegetation, the wind speed plays a larger role in the partitioning of available energy into sensible heat flux. This is because there is insufficient vegetation or moisture to facilitate higher latent heat flux, and the overall annual average wind speed is higher (around 4–6 m/s) in these regions relative to the tropical forests (wind speeds around 0–3 m/s). In these ways, wind speed plays a larger role in the aerodynamic resistance in these regions. In comparing the sensitivity of the sensible heat flux to the wind speed with that of other studies, we find the average of three forest site sensitivities from simulated sensible heat flux in Alton et al. (2006) of 2.1 W/m² per m/s is very similar to the average at the same forest sites of 3.2 W/m² per m/s in our study.

The smallest sensitivity to all inputs at the northern high latitudes is likely due to the small relative magnitude of several inputs compared to other global regions. The average wind speed in this region is only 2–3 m/s, the average temperature gradient is between –2 and 0 °K, and the average C_{z11} is between 0.1 and 0.4. These low values combined with a moderate roughness length when averaged using fractional vegetated area for each cell at around 1.0 m results in no single input having a dominant influence on the magnitude of the sensible heat flux. This keeps the sensitivity of sensible heat flux to these inputs small. Additionally, the increase in sensitivity seen in eastern Russia and western Alaska to each of the inputs, compared with the remaining high latitude regions, is likely related to the change in values of several inputs between these two regions. Although the average wind speed remains the same in both regions, the average roughness length drops to under 0.1 in eastern Russia and under 0.8 in most of Alaska, the average temperature gradient increases to 0–2 °K, and the average C_{z11} jumps above 0.5—and as high as 1.4 in some small regions and even to 3 or 4 in other areas. The increase in C_{z11} , the increase in temperature gradient, and the decrease in roughness length all increase the sensitivity of sensible heat flux to each of these inputs in eastern Russia and western Alaska.

4.2. Uncertainty Analysis

Understanding the uncertainty in sensible heat flux is also important as it accounts for both the sensitivity and uncertainty in each input, all which contribute to the overall uncertainty of the sensible heat flux. The largest overall uncertainty in the Amazon seen in Figure 2 is attributed to the C_{z11} input, as seen in Figure 3a. This large uncertainty results from a combination of both a very high sensitivity of sensible heat flux to

change in C_{ztl} seen in Figure 1a and the large uncertainty in C_{ztl} relative to other regions due to a lack of eddy flux stations in South America that can be used to estimate C_{ztl} . The smallest overall uncertainty in middle to high latitudes in Eurasia, as seen in Figure 2, results from the small uncertainties in wind speed, roughness length, and C_{ztl} such that the primary contributor to the uncertainty in this region is the temperature gradient uncertainty. Although 90% of the uncertainty in this region is due to the temperature gradient, as seen in Figure 3b, the uncertainty in the temperature gradient is larger for other regions, and those larger values combined with larger relative uncertainties from the remaining three primary inputs cause the overall mid to high latitude uncertainty to be smaller in comparison.

The overall uncertainty between 25 and 35 W/m^2 , and the global average uncertainty of 24.8 W/m^2 is larger than the uncertainty range specified in the literature of 9 W/m^2 in Wild et al. (2015) and the uncertainty range of 4 W/m^2 in Jung et al. (2011), but it does compare with the full range of different estimates reported within the literature. As mentioned in section 1, Wild et al. (2015) reports a range of 27 W/m^2 between the lowest and highest estimates from Coupled Model Intercomparison Project Phase 5 models, and Jimenez et al. (2011) displays estimates ranging from 18 to 57 W/m^2 , which is a total range of 39 W/m^2 .

We can attribute the disparity in uncertainty in Figure 2 between the Congo and the Amazon as well as parts of Indonesia to the different sensitivities of the sensible heat flux to the input data. Figure 3c shows at least 90% of the uncertainty in the Amazon and portions of Indonesia is attributed to the C_{ztl} , while the uncertainty in the Congo is largely dominated by the impacts of the temperature gradient. These differences in uncertainty are also consistent with differences in the overall magnitude of higher sensible heat fluxes in the Amazon and lower sensible heat fluxes in the Congo (Siemann et al., 2018).

When comparing the magnitude of this sensible heat total uncertainty with uncertainty reported at the local scale, we find similarities between our estimates with Metzger et al. (2016) at the local scale. Metzger et al. (2016) reports an uncertainty of approximately 3.5 W/m^2 in the sensible heat flux at a natural peatland site in Degerö Stormyr, Sweden, and our sensible heat flux total uncertainty at the pixel over the same location is 5.8 W/m^2 . The difference of 2.3 W/m^2 could result from the discrepancies in the scale of the pixel to the local scale site of Metzger et al. (2016).

Of all the primary inputs, the largest fraction of the total uncertainty seen in Figure 3 is attributed to the uncertainty in the temperature gradient in most regions. The temperature gradient's dominant impact, relative to other inputs, is consistent with its expected influence as the dominant input in the denominator for sensible heat flux (see equation (7)). The influence of the temperature gradient, reflected in Figure 3b, at over 60–80% of the uncertainty in regions such as Australia, the Great Plains of CONUS, Southwest CONUS, the Horn of Africa, the Sahara, the Canadian Plains, and the Middle East is evident due to the differences in the sensible heat flux in products calculated with different temperature gradient products in Figure 2 of Siemann et al. (2018). The gradient's influential contribution to the uncertainty may also partially be attributed to the wider range in products from which we draw our temperature gradient uncertainty estimate. Compared with our assumption for roughness length uncertainty, the uncertainty resulting from the C_{ztl} estimates, and the three wind speed products used to estimate the uncertainty range in wind speed, we have a wider range of products available for the temperature gradient to provide this uncertainty estimate.

When looking at the relative uncertainty and coefficient of variation in Figure 4, we display the size of the uncertainties due to each input and the total uncertainty relative to the mean in the sensible heat flux. In this way, the higher coefficient of variation and relative uncertainty due to C_{ztl} in the Amazon consistently reflect the smaller mean sensible heat flux in relation to the uncertainty driven by the C_{ztl} . The larger coefficient of variation and relative uncertainty due to the temperature gradient in the northern high latitudes reflects the larger uncertainty relative to a small mean sensible heat flux in these regions. The lower relative uncertainties and coefficients in the Sahara, the Horn of Africa, Australia, Horn of Africa, and the Middle East reflect the higher sensible heat fluxes, which still dominate over the magnitude of the uncertainty. These lower coefficients of variation in Australia, the Sahara, the Middle East, and the Horn of Africa coincide with regions which are generally drier with more stable climates year round, so the variation could be expected to be smaller than regions such as the high latitudes with seasonal variation of snow cover or the Amazon with large fluctuations of moisture facilitating partitioning of available energy into latent heat flux from day to day in the tropics.

We did not assess additional sources of uncertainty noted in the introduction that impact the sensible heat flux, most prominently at the pixel, local, or regional scale. Tang and Li (2017) evaluate the sensitivity of evapotranspiration estimates from their end-member-based soil and vegetation energy partitioning approach due to inputs including fractional vegetation cover and vegetation height. While the radiation, air temperature, and surface temperature are among the most sensitive parameters, the fractional cover is among the moderately sensitive parameters, causing variations of up to 2 or 3% in the evapotranspiration due to a 20% change in fractional cover (Tang & Li, 2017). Although uncertainty in the vegetation height and fractional cover of vegetation can be quantified for a local study region, robust measures of the local-scale uncertainty in these parameters are difficult to obtain globally.

5. Conclusions

In this study, we evaluate the global sensitivity of the sensible heat flux from the core input data sets of the temperature gradient, the wind speed, the $C_{z_{il}}$, and the roughness length for momentum using methodology based on Chapra and Canale (2010). We use the sensitivity and the uncertainty in each input data set to calculate an overall sensible heat flux uncertainty using methodology based on Mays and Tung (1992). We find that the largest sensitivities to $C_{z_{il}}$ in regions of the Amazon, northern Australia, and the plains of North America, which are unique regions in the distribution of FLUXNET eddy flux towers from which the $C_{z_{il}}$ is derived. These regions also coincide with regions of mismatch between our sensible heat flux products, reanalysis products, and estimates from the literature, seen in Siemann et al. (2018). The sensible heat flux is most sensitive to the temperature gradient in drier regions of shorter vegetation, which are similar regions for the highest sensitivities to the roughness length for momentum and the wind speed. We find the smallest sensitivities of the sensible heat algorithm to all inputs in the northern high latitudes.

Accounting for both the sensitivity due to each input data set and the uncertainty in each input data set, we find the largest overall uncertainty in the Amazon of over 50–100 W/m² and the smallest overall uncertainty in the northern high latitudes of 5–10 W/m². The overall global average uncertainty of the sensible heat flux is computed to be 24.8 W/m², with most regions ranging from 25 to 35 W/m². Outside the Amazon and Indonesia where the $C_{z_{il}}$ contributes most to the uncertainty, the temperature gradient contributes most to the uncertainty in the sensible heat flux. Additionally, the coefficient of variation is largest in the Amazon, far northern high latitudes, and the Congo, in which the sensible heat flux estimates are small compared to the magnitude of the uncertainty. These global sensitivities and uncertainties enable us to know which regions our sensible heat flux estimates are most reliable, as well as which input data sets drive the uncertainty in the sensible heat flux, necessitating improvements in the data sets for these drivers to produce more accurate future estimates of sensible heat flux. Future work should include a focus on reducing the uncertainties in the individual input data sets, particularly the temperature gradient and the $C_{z_{il}}$, to reduce the uncertainty in future sensible heat flux estimates.

Acknowledgments

This work is supported by NOAA grant NA11OAR4310175. The data sets supporting these conclusions are available at http://hydrology.princeton.edu/~siemann/data/Sensitivity_Uncertainty/ and questions can be directed to the corresponding author, Amanda L. Siemann at siemann@princeton.edu.

References

- Alton, P., Mercado, L., & North, P. (2006). A sensitivity analysis of the land-surface scheme JULES conducted for three forest biomes: Biophysical parameters, model processes, and meteorological driving data. *Global Biogeochemical Cycles*, *20*, GB1008. <https://doi.org/10.1029/2005GB002653>
- Boisier, J. P., Noblet-Ducoudre, N. d., Pitman, A. J., Cruz, F. T., Delire, C., Hurk, B. J., et al. (2012). Attributing the impacts of land-cover changes in temperate regions on surface temperature and heat fluxes to specific causes: Results from the first LUCID set of simulations. *Journal of Geophysical Research*, *117*, D12116. <https://doi.org/10.1029/2011JD017106>
- Bormann, H. (2008). Sensitivity of a soil-vegetation-atmosphere-transfer scheme to input data resolution and data classification. *Journal of Hydrology*, *351*(1-2), 154–169. <https://doi.org/10.1016/j.jhydrol.2007.12.011>
- Bounoua, L., Masek, J., & Tourre, Y. M. (2006). Sensitivity of surface climate to land surface parameters: A case study using the simple biosphere model SiB2. *Journal of Geophysical Research*, *111*, D22S09. <https://doi.org/10.1029/2006JD007309>
- Cammalleri, C., Anderson, M. C., Ciraolo, G., D'Urso, G., Kustas, W., Loggia, G. L., & Minacapilli, M. (2012). Applications of a remote sensing-based two-source energy balance algorithm for mapping surface fluxes without in situ air temperature observations. *Remote Sensing of Environment*, *124*, 502–515. <https://doi.org/10.1016/j.rse.2012.06.009>
- Chaney, N. W., Herman, J. D., Ek, M. B., & Wood, E. F. (2016). Deriving global parameter estimates for the Noah Land Surface Model using FLUXNET and machine learning. *Journal of Geophysical Research: Atmospheres*, *121*, 13,218–13,235. <https://doi.org/10.1002/2016JD024821>
- Chapra, S., & Canale, R. P. (2010). *Numerical methods for engineers* (6th ed.). New York: McGraw Hill Higher Education.
- Chehbouni, A., Nouvellon, Y., Lhomme, J.-P., Watts, C., Boulet, G., Kerr, Y. H., et al. (2001). Estimation of surface sensible heat flux using dual angle observations of radiative surface temperature. *Agricultural and Forest Meteorology*, *108*(1), 55–65. [https://doi.org/10.1016/S0168-1923\(01\)00221-0](https://doi.org/10.1016/S0168-1923(01)00221-0)

- Clemen, R. T., & Winkler, R. L. (1999). Combining probability distributions from experts in risk analysis. *Risk Analysis*, 19(2), 187–203. <https://doi.org/10.1111/j.1539-6924.1999.tb00399.x>
- Coccia, G., Siemann, A. L., Pan, M., & Wood, E. F. (2015). Creating consistent datasets combining remotely-sensed data and land surface model estimates through a Bayesian uncertainty post-processing: The case of land surface temperature from HIRS. *Remote Sensing of Environment*, 170, 290–305. <https://doi.org/10.1016/j.rse.2015.09.010>
- Coccia, G., & Todini, E. (2011). Recent developments in predictive uncertainty assessment based on the model conditional processor approach. *Hydrology and Earth System Sciences*, 15(10), 3253–3274. <https://doi.org/10.5194/hess-15-3253-2011>
- Defries, R. S., Hansen, M. C., Townshend, J. R., Janetos, A. C., & Loveland, T. R. (2000). A new global 1-km dataset of percentage tree cover derived from remote sensing. *Global Change Biology*, 6(2), 247–254. <https://doi.org/10.1046/j.1365-2486.2000.00296.x>
- Dirmeyer, P. A., Ducharme, F. Z., Morrill, J. C., & Koster, R. D. (2000). The sensitivity of surface fluxes to soil water content in three land surface schemes. *Journal of Hydrometeorology*, 1(2), 121–134. [https://doi.org/10.1175/1525-7541\(2000\)001%3C0121:TSOSFT%3E2.0.CO;2](https://doi.org/10.1175/1525-7541(2000)001%3C0121:TSOSFT%3E2.0.CO;2)
- Ek, M. B., Mitchell, K. E., Lin, Y., Rogers, E., Grunmann, P., Koren, V., et al. (2003). Implementation of Noah land surface model advances in the National Centers for Environmental Prediction operational Eta model. *Journal of Geophysical Research*, 108(D22), 8851. <https://doi.org/10.1029/2002JD003296>
- FLUXNET web page (2016). O. DAAC, producer. Retrieved from <http://fluxnet.ornl.gov>
- Gibson, L. A., Munch, Z., & Engelbrecht, J. (2011). Particular uncertainties encountered in using a pre-packaged SEBS model to derive evapotranspiration in a heterogeneous study area in South Africa. *Hydrology and Earth System Sciences*, 15(1), 295–310. <https://doi.org/10.5194/hess-15-295-2011>
- Hansen, M., Defries, R. S., Townshend, J., & Sohlberg, R. (2000). Global land cover classification at 1 km spatial resolution using a classification tree approach. *International Journal of Remote Sensing*, 21(6-7), 1331–1364. <https://doi.org/10.1080/014311600210209>
- Hou, Z., Huang, M., Leung, L., Lin, G., & Ricciuto, D. (2012). Sensitivity of surface flux simulations to hydrologic parameters based on an uncertainty quantification framework applied to the Community Land Model. *Journal of Geophysical Research*, 117, D15108. <https://doi.org/10.1029/2012JD017521>
- Janjic, Z. I. (1994). The Step-Mountain Eta Coordinate Model: Further developments of the convection, viscous sublayer, and turbulence closure schemes. *Monthly Weather Review*, 122(5), 927–945. [https://doi.org/10.1175/1520-0493\(1994\)122%3C0927:TSMECM%3E2.0.CO;2](https://doi.org/10.1175/1520-0493(1994)122%3C0927:TSMECM%3E2.0.CO;2)
- Jimenez, C., Prigent, C., Mueller, B., Seneviratne, S. I., McCabe, M. F., Wood, E. F., et al. (2011). Global intercomparison of 12 land surface heat flux estimates. *Journal of Geophysical Research*, 116, D02102. <https://doi.org/10.1029/2010JD014545>
- Jung, M., Reichstein, M., Margolis, H. A., Cescatti, A., Richardson, A. D., Arain, M. A., et al. (2011). Global patterns of land-atmosphere fluxes of carbon dioxide, latent heat, and sensible heat derived from eddy covariance, satellite, and meteorological estimates. *Journal of Geophysical Research*, 116, G00J07. <https://doi.org/10.1029/2010JG001566>
- Long, D., Singh, V. P., & Li, Z.-L. (2011). How sensitive is SEBAL to changes in input variables, domain size and satellite sensor? *Journal of Geophysical Research*, 116, D21107. <https://doi.org/10.1029/2011JD016542>
- Madhusoodhanan, C., Sreeja, K., & Eldho, T. (2017). Assessment of uncertainties in global land cover products for hydro-climate modeling in India. *Water Resources Research*, 53, 1713–1734. <https://doi.org/10.1002/2016WR020193>
- Marx, A., Kunstmann, H., Schuttemeyer, D., & Moene, A. F. (2008). Uncertainty analysis for satellite derived sensible heat fluxes and scintillometer measurements over Savannah environment and comparison to mesoscale meteorological simulation results. *Agricultural and Forest Meteorology*, 148(4), 656–667. <https://doi.org/10.1016/j.agrformet.2007.11.009>
- Mays, L. W., & Tung, Y.-K. (1992). *Hydrosystems engineering and management*. New York: McGraw-Hill, Inc.
- Metzger, C., Nilsson, M., Peichl, M., & Jansson, P. (2016). Parameter interactions and sensitivity analysis for modelling carbon heat and water fluxes in a natural peatland, using CoupModel v5. *Geoscientific Model Development*, 9(12), 4313–4338. <https://doi.org/10.5194/gmd-9-4313-2016>
- Monin, A. S., & Obukhov, A. M. (1954). Basic laws of turbulent mixing in the surface layer of the atmosphere. *Contributions of the Geophysical Institute of the Slovak Academy of Sciences*, 24, 163–187.
- Monteith, J. L. (1973). *Principles of Environmental Physics*. London: Edward Arnold.
- Norman, J. M., Divakarla, M., & Goel, N. S. (1995). Algorithms for extracting information from remote thermal-IR observations of the earth's surface. *Remote Sensing of Environment*, 51(1), 157–168. [https://doi.org/10.1016/0034-4257\(94\)00072-U](https://doi.org/10.1016/0034-4257(94)00072-U)
- Oleson, K. W., & Bonan, G. B. (2008). An urban parameterization for a global climate model. Part II: Sensitivity to input parameters and the simulated urban Heat Island in offline simulations. *Journal of Applied Meteorology and Climatology*, 47(4), 1061–1076. <https://doi.org/10.1175/2007JAMC1598.1>
- Pipunic, R. C., Walker, J. P., & Western, A. (2008). Assimilation of remotely sensed data for improved latent and sensible heat flux prediction: A comparative synthetic study. *Remote Sensing of Environment*, 112(4), 1295–1305. <https://doi.org/10.1016/j.rse.2007.02.038>
- Ren, H., Liang, S., Yan, G., & Cheng, J. (2013). Empirical algorithms to map global broadband emissivities over vegetated surfaces. *IEEE Transactions on Geoscience and Remote Sensing*, 51(5), 2619–2631. <https://doi.org/10.1109/TGRS.2012.2216887>
- Rosolem, R., Gupta, H. V., Shuttleworth, W. J., Zeng, X., & Goncalves, L. G. (2012). A fully multiple-criteria implementation of the Sobol' method for parameter sensitivity analysis. *Journal of Geophysical Research*, 117, D07103. <https://doi.org/10.1029/2011JD016355>
- Saha, S., Moorthi, S., Pan, H.-L., Wu, X., Wang, J., Nadiga, S., et al. (2010). The NCEP climate forecast system reanalysis. *Bulletin of the American Meteorological Society*, 91(8), 1015–1058. <https://doi.org/10.1175/2010B>
- Sanchez, J. M., Kustas, W. P., Caselles, V., & Anderson, M. C. (2008). Modelling surface energy fluxes over maize using a two-source patch model and radiometric soil and canopy temperature observations. *Remote Sensing of Environment*, 112(3), 1130–1143. <https://doi.org/10.1016/j.rse.2007.07.018>
- Schulz, K., & Beven, K. (2003). Data-supported robust parameterisations in land surface-atmosphere flux predictions: Towards a top-down approach. *Hydrological Processes*, 17(11), 2259–2277. <https://doi.org/10.1002/hyp.1331>
- Sellers, P. J., Hall, F. G., Kelly, R. D., Black, A., Baldocchi, D., Berry, J., et al. (1997). BOREAS in 1997: Experiment overview, scientific results, and future directions. *Journal of Geophysical Research*, 102(D24), 28,731–28,769. <https://doi.org/10.1029/97JD03300>
- Sheffield, J., Goteti, G., & Wood, E. F. (2006). Development of a 50-year high-resolution global dataset of meteorological forcings for land surface modeling. *Journal of Climate*, 19(13), 3088–3111. <https://doi.org/10.1175/JCLI3790.1>
- Siemann, A. L., Chaney, N., & Wood, E. F. (2018). Development and validation of a long term, global, terrestrial sensible heat flux dataset. *Journal of Climate*. <https://doi.org/10.1175/JCLI-D-17-0732.1>
- Siemann, A. L., Coccia, G., Pan, M., & Wood, E. F. (2016). Development and analysis of a long-term, global, terrestrial land surface temperature dataset based on HIRS satellite retrievals. *Journal of Climate*, 29(10), 3589–3606. <https://doi.org/10.1175/JCLI-D-15-0378.1>
- Stone, M. (1961). The opinion pool. *The Annals of Mathematical Statistics*, 32(4), 1339–1342. <https://doi.org/10.1214/aoms/117704873>

- Tang, R., & Li, Z.-L. (2017). An end-member-based two-source approach for estimating land surface evapotranspiration from remote sensing data. *IEEE Transactions on Geoscience and Remote Sensing*, *55*(10), 5818–5832. <https://doi.org/10.1109/TGRS.2017.2715361>
- Tang, R., Li, Z.-L., Chen, K.-S., Jia, Y., Li, C., & Sun, X. (2013). Spatial-scale effect on the SEBAL model for evapotranspiration estimation using remote sensing data. *Agriculture and Forest Meteorology*, *174–175*, 28–42. <https://doi.org/10.1016/j.agrformet.2013.01.008>
- Tang, R., Li, Z.-L., & Tang, B. (2010). An application of the Ts–VI triangle method with enhanced edges determination for evapotranspiration estimation from MODIS data in arid and semi-arid regions: Implementation and validation. *Remote Sensing of Environment*, *114*(3), 540–551. <https://doi.org/10.1016/j.rse.2009.10.012>
- Timmermans, W. J., Kustas, W. P., Anderson, M. C., & French, A. N. (2007). An intercomparison of the Surface Energy Balance Algorithm for Land (SEBAL) and the Two-Source Energy Balance (TSEB) modeling schemes. *Remote Sensing of Environment*, *108*(4), 369–384. <https://doi.org/10.1016/j.rse.2006.11.028>
- Todini, E. (2008). A model conditional processor to assess predictive uncertainty in flood forecasting. *International Journal of River Basin Management*, *6*(2), 123–137. <https://doi.org/10.1080/15715124.2008.9635342>
- Wang, A., & Zeng, X. (2013). Development of global hourly 0.5° land surface air temperature datasets. *Journal of Climate*, *26*(19), 7676–7691. <https://doi.org/10.1175/JCLI-D-12-00682.1>
- Wang, Y. Q., Xiong, Y. J., Qiu, G. Y., & Zhang, Q. T. (2016). Is scale really a challenge in evapotranspiration estimation? A multi-scale study in the Heihe oasis using thermal remote sensing and the three-temperature model. *Agricultural and Forest Meteorology*, *230–231*, 128–141. <https://doi.org/10.1016/j.agrformet.2016.03.012>
- Wild, M., Folini, D., Hakuba, M. Z., Schar, C., Seneviratne, S. I., Kato, S., et al. (2015). The energy balance over land and oceans: An assessment based on direct observations and CMIP5 climate models. *Climate Dynamics*, *44*(11–12), 3393–3429. <https://doi.org/10.1007/s00382-014-2430-z>
- Xu, K., Metzger, S., & Desai, A. (2017). Upscaling tower-observed turbulent exchange at fine spatio-temporal resolution using environmental response functions. *Agricultural and Forest Meteorology*, *232*, 10–22. <https://doi.org/10.1016/j.agrformet.2016.07.019>
- Zhan, X., Kustas, W. P., & Humes, K. S. (1996). An intercomparison study on models of sensible heat flux over partial canopy surfaces with remotely sensed surface temperature. *Remote Sensing of Environment*, *58*(3), 242–256. [https://doi.org/10.1016/S0034-4257\(96\)00049-1](https://doi.org/10.1016/S0034-4257(96)00049-1)
- Zhang, K., Ma, J., Zhu, G., Ma, T., Han, T., & Feng, L. L. (2017). Parameter sensitivity analysis and optimization for a satellite-based evapotranspiration model across multiple sites using Moderate Resolution Imaging Spectroradiometer and flux data. *Journal of Geophysical Research: Atmospheres*, *122*, 230–245. <https://doi.org/10.1002/2016JD025768>
- Zilitinkevich, S. S. (1995). Non-local turbulent transport: Pollution dispersion aspects of coherent structure of convective flows. In H. Power, N. Moussiopoulos, & C. A. Brebbia (Eds.), *Air pollution III-volume I. Air pollution theory and simulation* (pp. 53–60). Southampton, Boston: Computational Mechanics Publications.